

Accepted Manuscript

An analysis of macro- and micro-scale residual stresses of Type I, II and III using FIB-DIC micro-ring-core milling and crystal plasticity FE modelling

E. Salvati, A.M. Korsunsky



PII: S0749-6419(17)30137-7

DOI: [10.1016/j.ijplas.2017.07.004](https://doi.org/10.1016/j.ijplas.2017.07.004)

Reference: INTPLA 2223

To appear in: *International Journal of Plasticity*

Received Date: 21 March 2017

Revised Date: 29 June 2017

Accepted Date: 10 July 2017

Please cite this article as: Salvati, E., Korsunsky, A.M., An analysis of macro- and micro-scale residual stresses of Type I, II and III using FIB-DIC micro-ring-core milling and crystal plasticity FE modelling, *International Journal of Plasticity* (2017), doi: 10.1016/j.ijplas.2017.07.004.

This is a PDF file of an unedited manuscript that has been accepted for publication. As a service to our customers we are providing this early version of the manuscript. The manuscript will undergo copyediting, typesetting, and review of the resulting proof before it is published in its final form. Please note that during the production process errors may be discovered which could affect the content, and all legal disclaimers that apply to the journal pertain.

Table 1. *Type II+III and Type III Standard Deviation values*

RS Type [MPa] Technique	II+III	III
FIB-DIC	41	-
FIB-DIC (incl. measurement error)	53	-
CP-FEM (untextured material)	75	66
CP-FEM (textured material)	70	56

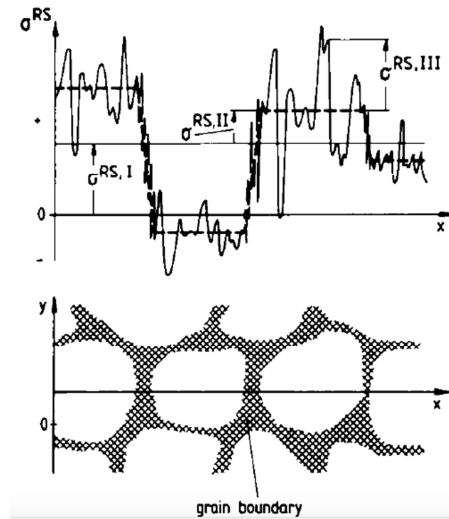


Fig.1. Illustration of the multi-scale nature of residual stresses in polycrystals (Reproduced with permission from [7]).

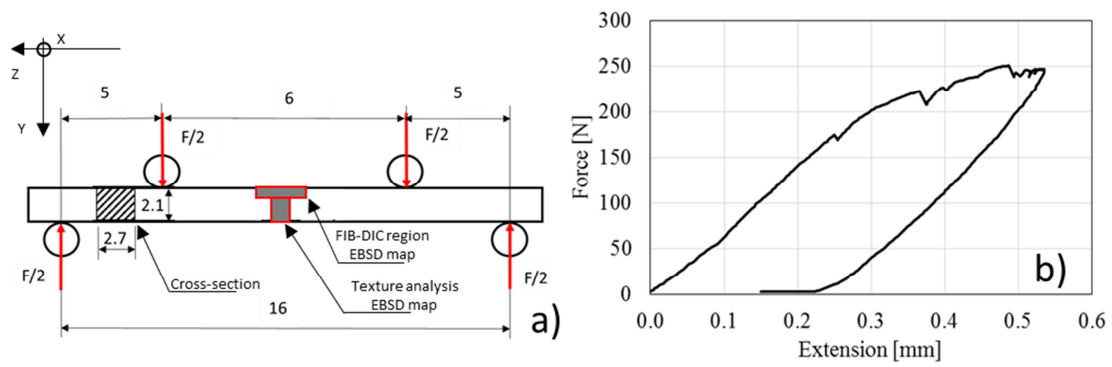


Fig.2 Bending test. a) Four-point bending experiment schematic illustration. Dimensions in millimetres. b) Force-extension curve recorded during four-point bending load application and removal.

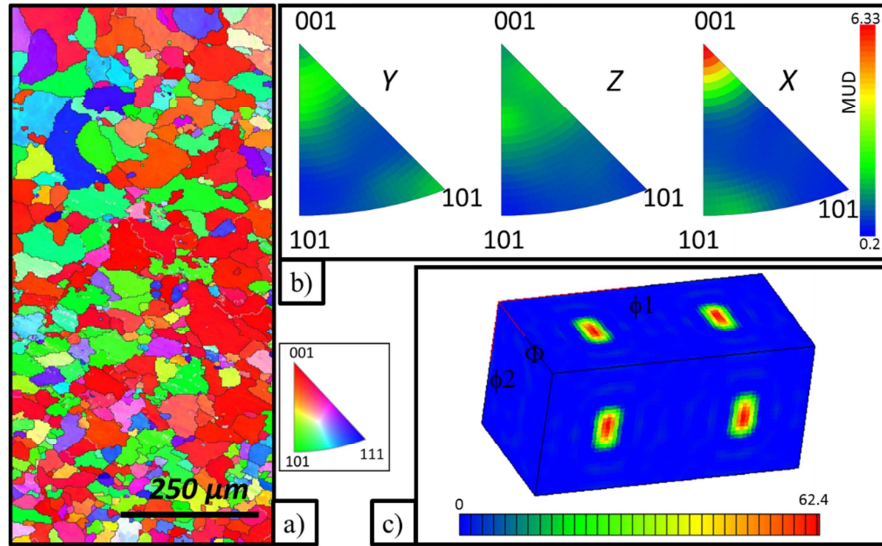


Fig.3 EBSD texture analysis. a) Orientation map IPF-X. b) Inverse Pole Figures. The colour bar is given in terms of the multiple of uniform density (m.u.d.). c) Orientation Distribution Function (ODF) contour plot.

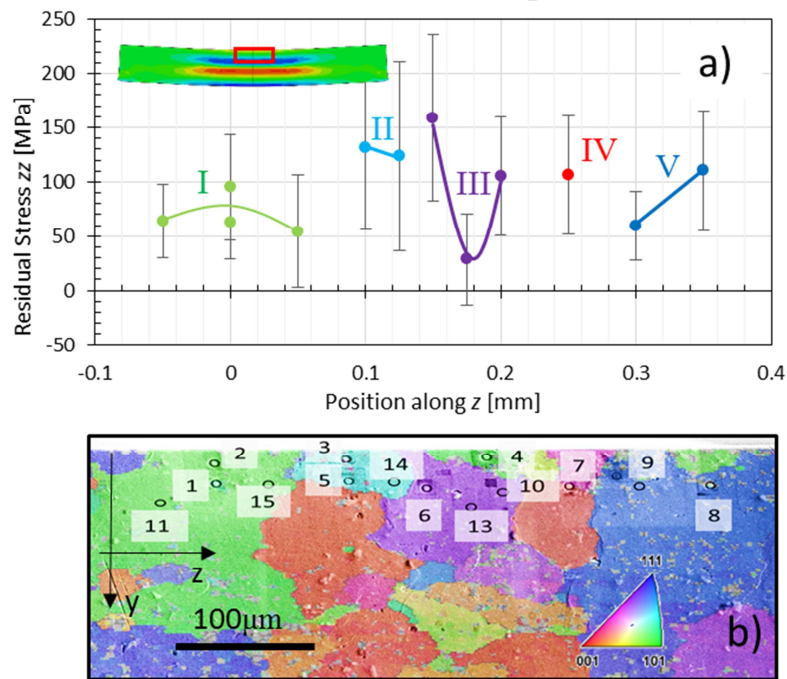


Fig. 4 Results of experimental of RS component σ_{zz} in the first region of interest. (a) Plot of the longitudinal RS component σ_{zz} for the grains identified in (b) EBSD grain orientation map.

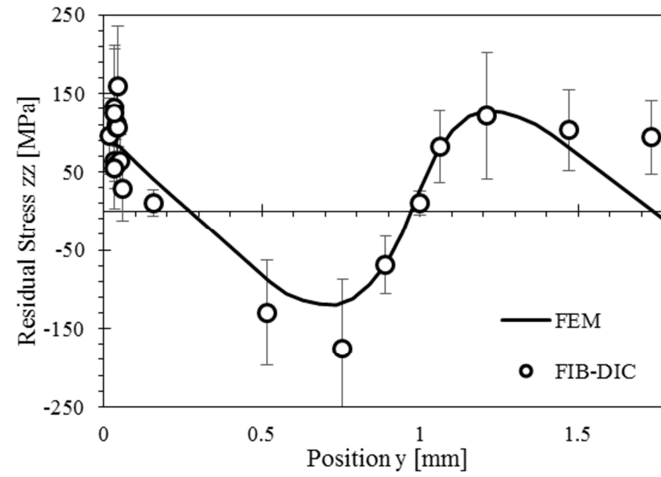


Fig.5 Experimentally determined RS variation across the beam (markers with error bars) plotted together with continuum FE prediction for macroscopic RS profile (solid curve).

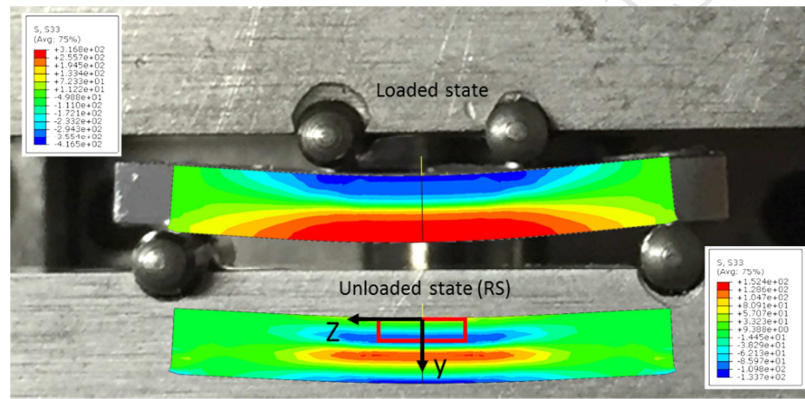


Fig.6 Beam curvature and superposition with FEM simulation at the maximum load applied. The contour plots show the σ_{zz} RS component. The contour plot at the bottom is superimposed on the the unloaded beam contour. The red rectangle indicates the region for EBSD mapping.

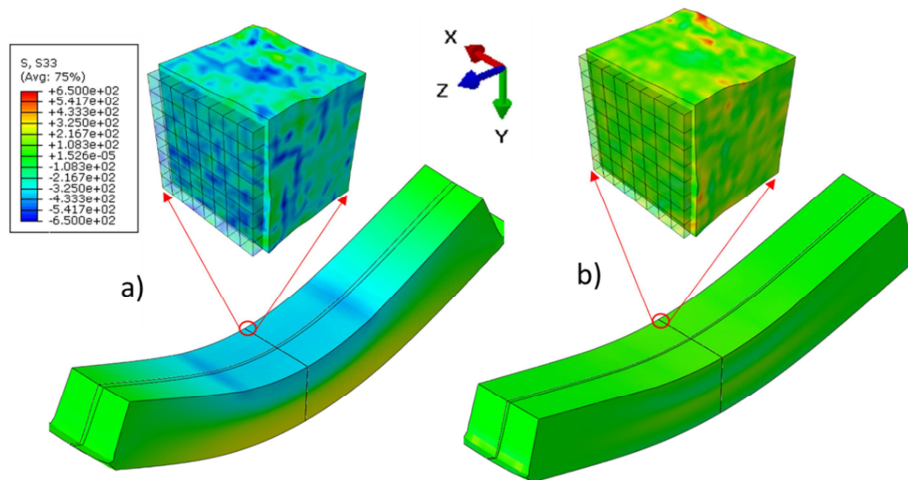


Fig.7. Illustration of stress contours from multi-scale FEM coupled simulation for an un-textured material. a)

Loaded configuration at the maximum load. b) Unloaded configuration.

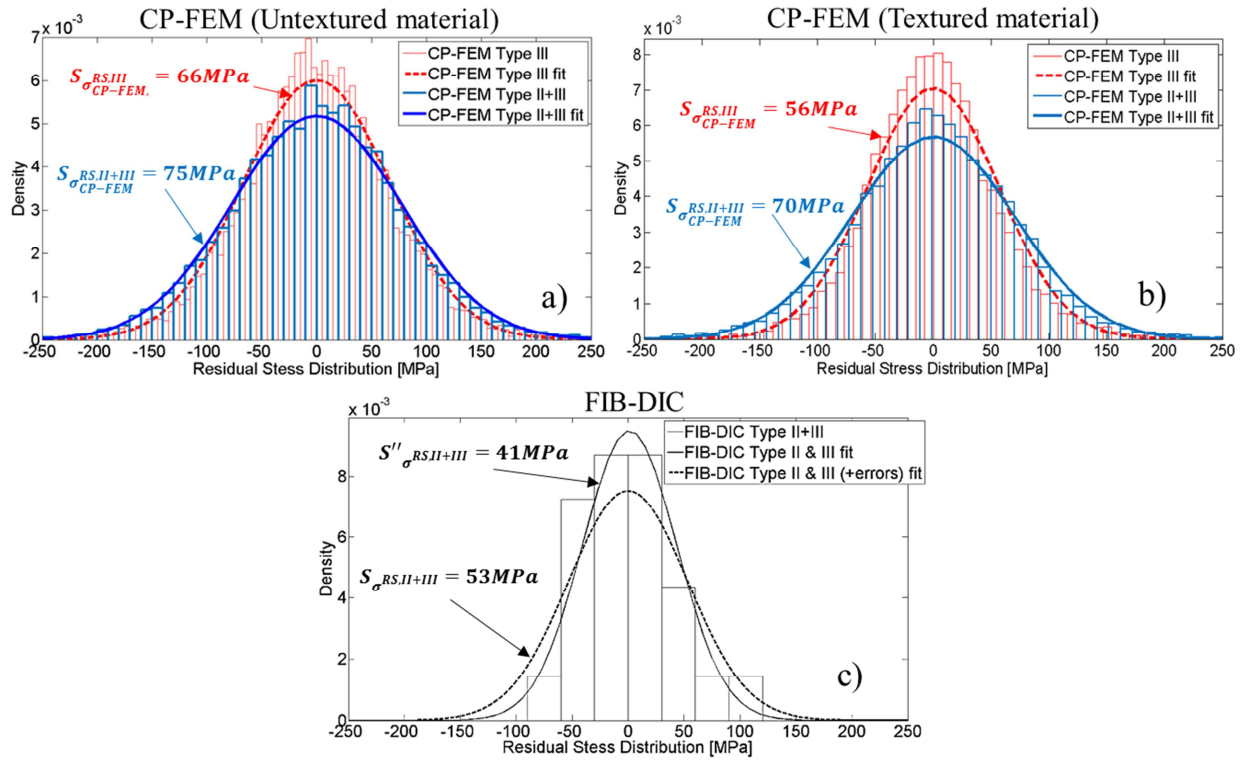


Fig.8. Probability density functions derived for the distributions of residual stress values obtained from a) CP-FEM simulation for an untextured polycrystalline material, b) CP-FEM simulation for the textured rolled Al plate and c) FIB-DIC experimental evaluation.

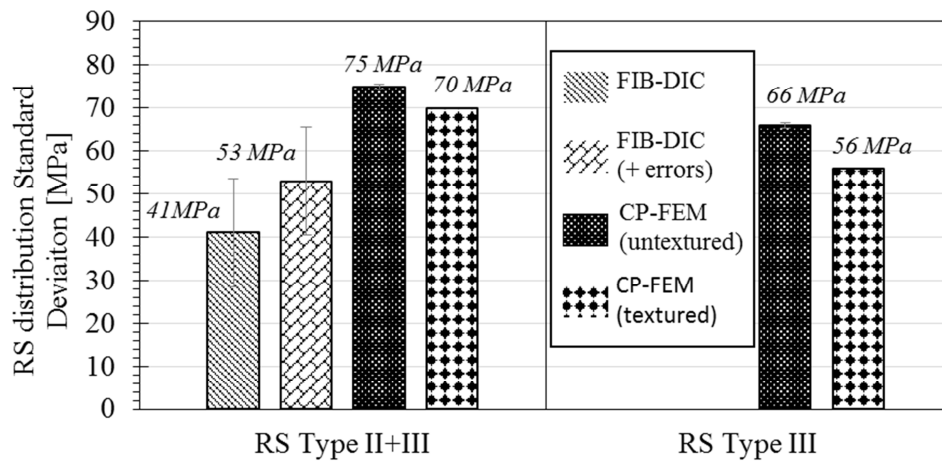


Fig.9. Residual Stress Standard Deviations comparison.

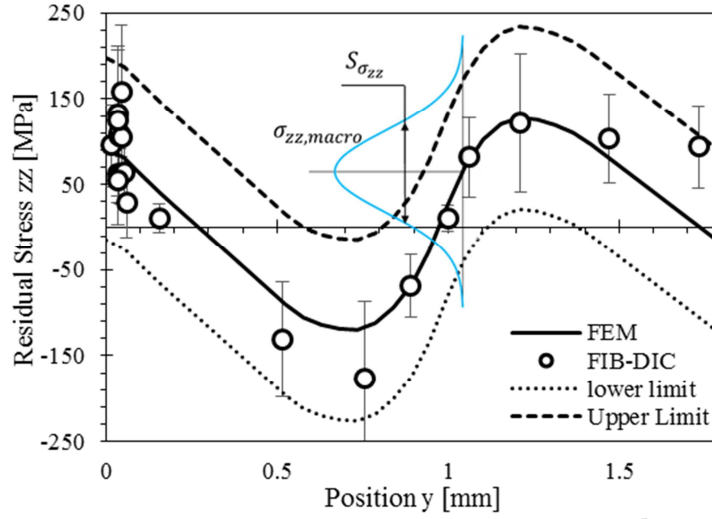


Fig.10. Experimental RS measurement (FIB-DIC) and simulation (CP-FEM) prediction. The Upper and Lower limits define the band at 95% of confidence. An example of normal distribution is shown by the blue continuous line.

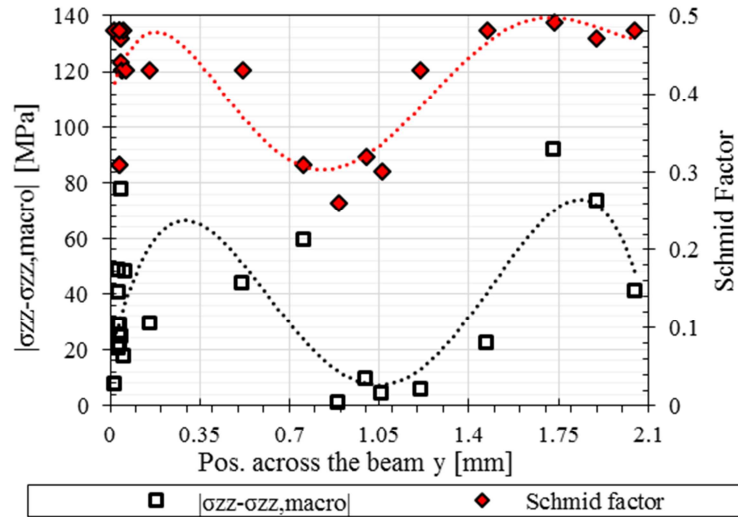


Fig.11 Measured RS deviation from the macroscopic prediction (lower curve and square markers) and the corresponding Schmid factor values (upper curve and diamond markers).

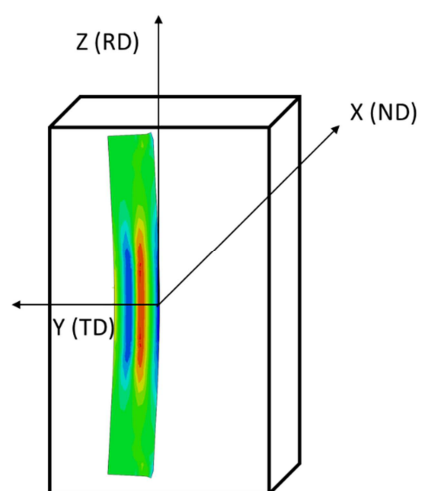


Fig. 12. Sample orientation with respect to the EBSD coordinate system.

- We experimentally measured the intragranular residual stress using the FIB-DIC ring-core technique.
- A Multi-scale FEM simulation approach was employed for the study of residual stress across the scales (Residual Stress type I, II & III).
- The statistical distribution of residual stress at the three length scales was evaluated regarding both experimental and numerical outcomes.
- The local Schmid factor was evaluated in order to check the correlation with the statistical stress distributions.

An Analysis of Macro- and Micro-Scale Residual Stresses of Type I, II and III Using FIB-DIC Micro-Ring-Core Milling and Crystal Plasticity FE Modelling

E. Salvati & A.M. Korsunsky

MBLEM – University of Oxford, Department of Engineering Science, Parks Road, OX1 3PJ, Oxford, United Kingdom

Table of Contents

Keywords	1
Abstract	1
1. Introduction	2
2. Sample and Test Setup Description.....	8
3. EBSD and FIB-DIC micro-ring-core analyses.....	9
4. Finite Element Analysis	12
4.1 Macro-scale simulation	12
4.2 Crystal Plasticity simulation.....	13
5. Statistical Analysis of RS Distribution.....	14
6. Influence of the Crystal Orientation on RS Development.....	18
7. Conclusions	20
Acknowledgements	21
Appendix – orientation convention for Schmid factor calculation	22
References	22

Keywords

Residual stress, statistical distribution, FIB-DIC, FEM

Abstract

Mechanical failure frequently initiates at the grain level, at which intra-granular stresses are of paramount importance. Under cyclic loading conditions regions within grains that experience high values of tensile residual stress are more prone to damage processes that lead to the formation of slip bands, defects, micro-voids and fissures that lead to crack nucleation and propagation. For these reasons,

the knowledge and understanding of residual stress across the scales (Types I, II and III) is crucial for improving the accuracy of mechanical failure prediction.

The present study was carried out with the purpose of revealing the presence and nature of inter- and intra-granular residual stresses (known as Type II and III) that were present in an Aluminium alloy sample as consequence of plastic deformation. To this end, a well-defined macroscopic residual stress field was introduced in a miniature four-point bent beam. Following sample microstructure mapping by EBSD, the evaluation of Type II & III residual stress at the grain level was conducted using FIB-DIC micro-ring-core method. The combination of two calibrated models at different length scales enabled the simulation of stress across the scales, from the continuum large scale down to the crystal level (CP-FEM). As the outcome of this multi-scale modelling, the RS simulation predictions at all scales (Type I, II & III) were obtained and compared with the experimental results using a statistical approach. A key significance of the finding was that the Standard Deviation of the local residual stress values (95% confidence interval half width) amounted to as much as $2/3$ of the macroscopic Type I value. This highlights the importance of including the information about Type II+III stresses in predictive design for structural integrity and the avoidance of failure.

Error propagation due to measurement uncertainty was accounted in the analysis. By considering Schmid factor at locations of residual stress measurement, a modest correlation was found with Type II & III residual stresses.

1. Introduction

Residual stress is a quantity of great complexity, not only due to its inherent tensorial nature, but also because of the dependence on the scale of consideration. The very definition of stress as a component of internal force per cross-sectional area introduces the concept of scale: the choice of the linear dimension to which this definition refers immediately engenders the inherent resolution of subsequent consideration. Notably, this also contains an element of non-locality: the operation involved in the definition of stress amounts to averaging over the chosen facet, implying that oscillations on the finer scale are deliberately ignored, but rather that the value obtained is distributed uniformly over the entire domain. It is worth noting, in passing, that a similar consideration applies to the definition of strain that is linked to initial reference length.

The natural limit to these definitions arises from the atomic structure of matter: once the characteristic dimension of the analysis becomes comparable with the interatomic distance (be it in crystalline or amorphous solid), the underlying ‘graininess’ of matter commands that bonding forces are taken into consideration in place of ‘smeared’ continuum description. An interesting set of challenges then arises in determining the extent to which continuum theories are capable of capturing correctly the mechanical interactions that play out at those shortest length scales. Seeking answers to these questions has been a persistent theme in nano-scale materials science and technology, and both bottom-up and top-down approaches have been pursued. Notable work in this field has been linked to the interpretation of molecular dynamics (MD) simulation results in terms of continuum stresses and strains [1-3].

As long as the scale of consideration remains above the scale of several interatomic distances, i.e. a few nanometres, the possibility of interrogating internal forces and deformation using classical continuum definitions of stress and strain remains valid and relevant [4]. It has been shown in various studies that tiny volumes of material as small as 3-4 atoms along the edge obey the classical laws of continuum mechanics, provided a correction is made for the surface energy effects that become significant at these scales [5].

In the context of residual stresses that are the principal topic of the present article this means that consideration can be conducted across the scales, from nanometric to microscopic to macro-scale. In relation to the underlying microstructure of polycrystalline solids this subject has been the focus of interest of several authors since the 1960’s, with notable contributions made by Macherauch [6], Pintschovius [7], Niku-Lari et al [8]. It was probably Macherauch who introduced the classification of residual stresses according to scale into Type I, II and III. Referring to the conceptual illustration of this classification in Fig.1 (from [8]), we note that the separation of stresses into these three types is *additive*, namely:

$$\sigma^{RS} = \sigma^{RS,I} + \sigma^{RS,II} + \sigma^{RS,III}. \quad (1)$$

This classification is of great importance both from the viewpoint of historical developments in residual stress analysis and evaluation methodology, and in terms of adopting correct approach and interpretation based in current research. Fig.1 shows the sample in the unloaded configuration that nevertheless contains macroscopic ($\sigma^{RS,I}$) and microscopic residual stresses. It illustrates that each

subsequent stress term refers to the *finer scale deviation* from the previous: Type II stresses refer to the extent to which the grain average value of residual stress differs from the macroscopic trend of Type I long range stresses, while Type III is the intragranular deviation of nanoscale stress from the grain average level. Type III stresses are of particular conceptual importance, since they may be directly associated with material defects, such as vacancies, voids, precipitates, inclusions, slip bands, dislocation pile-ups, etc. Although such straightforward association is not possible for Type II and Type I stresses, it is clear that these stresses arise due to aggregation of nano-scale defects that cause micro-scale mismatch in the thermal and mechanical properties between different distinct phases present within the material (Type II) or to macro-scale inhomogeneities associated with inelastic deformation history, e.g. bending, forging, machining, etc.

<< Figure 1 here >>

The present model is closely related to another well-known model widely accepted by the scientific community, the so-called Mughrabi composite model [9, 10]. Its basic idea is that the presence of dislocation distributions within a crystal makes it display some aspects of dual-phase (or multi-phase, in general) material behaviour that contains “hard” regions and “soft” regions. This model can be thought of as the combination of material unit cells, or representative volume elements (RVE’s) containing *walls* of high dislocation density (hard region) around the *cell core* region of low dislocation density (soft region). As well as the description discussed above, the Mughrabi composite model also introduces built-in *long-range* internal stresses. Considering the material configuration after loading, the model predicts high and low magnitudes of residual stress, respectively in the hard and soft regions. It is then evident that the smallest scale considered in the model determines the RS types referred to in terms of the grain level (e.g. *intra-* vs *inter-*).

All of these processes and sources of residual stress can be conveniently generalised based on the scale-independent concept of *eigenstrain* that refers to any inelastic process, including phase transformation, plastic deformation, etc. The development of eigenstrain theory [11-17] led to the formulation of direct and inverse problems that allow, respectively, the calculation of residual stress from the underlying intrinsic eigenstrain distribution, or the determination of unknown eigenstrain distribution based on residual stress known at a number of probe points.

Accurate and reliable residual stress (RS) evaluation is a critical pre-requisite step for understanding and predicting engineering component behaviour and failure. Quantification of the magnitude and orientation and fine scale variation of locked-in internal forces has great utility for a wide range of applications, from the impact of ion radiation on thin films to the interaction between residual and applied stresses in the failure mode of high-pressure components.

Type II and III stresses are usually neglected when dealing with the study of the structural integrity of mechanical components having characteristic dimensions of the order of tens of millimetres. Nevertheless, it is evident that mechanical failure originates at the grain level, where intra-granular stress plays a crucial role. Particularly when cyclic loading is applied, regions within grains that contain tensile RS are more prone to damage accumulation in the form of slip or twinning, subsequent formation of defects and micro-voids that lead to crack nucleation and propagation. A relevant example can be the dwell fatigue failure which is a well-known failure mechanism experienced in aero-engine discs. This type of failure manner is thought to be highly influenced by the presence of very localised residual stress arising by the interaction between hard and soft grains during cycling [18], giving rise eventually to facet formations followed by crack nucleation.

For these reasons, the knowledge and understanding of Type III RS has the potential to improve dramatically the accuracy of mechanical failure prediction. From the practical point of view, precise point-wise RS simulation within material microstructure remains rather prohibitive due to the large computational effort required. On the other hand, a statistical approach to the problem may provide an improvement in terms of accounting for the influence of RS distribution on the onset and development of failure processes.

Whilst the evaluation methods of Type I residual stress have advanced to the stage when industry level standards have been available for a few decades, until recently intergranular (Type II) and intragranular residual stresses (Type III) continued to be discussed and described mostly at the conceptual level. This is due to the insurmountable difficulties of their practical evaluation at the appropriate scale and resolution. Experimental stress evaluation techniques are inextricably linked to a certain length scale, the so-called *gauge volume*, within which the interaction between the probe and the solid material in question is played out. In terms of the experimental techniques available for RS

evaluation, attention must be paid to the effective gauge volume and nature of measurement. It is important to make a further classification of RS analysis techniques into three principal approaches:

- I. *Non-destructive.* Physical analysis methods allow RS evaluation via the quantification of small variations in structural or physical parameters e.g. the evaluation of interplanar atomic lattice spacing by diffraction, or changes in molecular bond stiffness by spectroscopy. The wide range of experimental methods includes high resolution optical techniques, Raman spectroscopy analysis of diamond-like coatings [19, 20] and a multitude of X-ray diffraction techniques for the analysis of intergranular stresses [21-27]. High resolution Electron Back Scatter Diffraction (HR-EBSD) has also made significant advances, and provides a powerful means of determining the lattice strains at resolutions ranging from sub-micron scale in back-scattered geometry to a few nm in transmission. In the last decade ever increasing levels of EBSD sensitivity have been achieved through the improvement of interpretation procedures [28]. Accurate intragranular lattice mis-orientation and quantitative RS analysis is now possible to quantify small changes in diffraction patterns (HR-EBSD) [29-33]. An example of recent relevant work is the analysis of intragranular stress/strain distribution around an inclusion [34]. Non-destructive methods rely on the quantification of the relative changes in the measured parameters, and require comparison with a reference. The accuracy of these techniques is therefore limited by the precision to which reliable reference values can be determined. However, this approach cannot be applied to amorphous materials or heavily deformed crystals, due to the degradation of Kikuchi scattering patterns.
- II. *Destructive.* The introduction of traction-free surfaces by sample sectioning induces stress redistribution and strain relief in the surrounding material. In this respect the approach is most closely related directly to the conventional definition of stress. The quantification of strain or displacement caused by the relief of tractions at the sectioned surface can be used in combination with numerical modelling to back-calculate the residual stresses originally present in the material. Experimental techniques that rely upon this approach include the slitting and contour method, with typical resolution in the range of fractions of a millimetre being achievable [35, 36].

III. *Semi-destructive*. The introduction of localised stress relief through hole-drilling or core milling can be used to quantify the magnitude of stress at a particular location within a sample [37, 38], whilst introducing minimal disturbance to its overall state. Similarly to the destructive techniques, the quantification of the strain change induced at the surface enables back-calculation of the residual stresses originally present. Traditional semi-destructive techniques are capable of resolving stress at the resolution of ~ 1 mm laterally, and at a depth resolution of ~ 0.03 mm. The idea of obtaining a minimally destructive probe of local RS using a ring-core geometry is not new: it goes back to the pioneering work of Wolf in the early 1970's [39]. The need for probing RS at smaller scales pushed researchers to develop procedures that involve finer tools for material removal [40-42]. The nano-scale Focused Ion Beam (FIB) [43] ring-core milling, in combination with Digital Image Correlation (DIC) has been developed to quantify RS in a precisely defined micro-scale gauge volume. Comparison with Finite Element (FE) simulation is used to relate the strain relief to the pre-existing RS state. FIB-DIC, as the method has become to be known in short, provides a conceptually appealing mechanistic approach to RS evaluation on the scale from a few microns to sub-micron, and thus lends itself naturally to the application for the study of inter- and intra-granular residual stresses (Type II and Type III).

The present work is aimed at evaluating and quantifying the scatter of intra- and inter-granular RS (Type II and III) within a polycrystalline material, in the specific case where the macroscopic RS (Type I) is well known. In order to perform the study, a miniature bent beam with a well-known macroscopic RS distribution was prepared. The sample was machined from an aluminium alloy plate and plastically deformed through the application of bending in the four-point configuration. In this way, the middle section of the beam was subjected to uniform bending moment associated with the same magnitude of plastic deformation (eigenstrain), that upon unloading generated Type I macroscopic residual stress that was uniform along the beam length, and varied only as a function of one coordinate transverse to the beam extent. Based on the macroscopic stress-strain curve evaluation, a numerical FE model was set up to assess the RS field arising after deformation. In order to establish the connection with micro-scale RS in the simulation, the deformation field obtained from macro-scale analysis served then as input (boundary conditions) for a Crystal Plasticity FEM model (CP-FEM). The combination of models at

different length scales enabled the simulation of stress across the scales, from the continuum large scale down to the crystal level. As the outcome of this multi-scale modelling, the RS simulation predictions across the scales (Type I, II & III) can be compared with experimental results.

To this end, EBSD and the FIB-DIC micro-ring-core method were employed for the evaluation of local crystal orientation/grain discrimination and RS evaluation, respectively. The knowledge of grain orientation allowed extracting information regarding the Schmid factor of each probed grain with respect to the principal loading direction (along the beam extent), with the view to elucidating the correlation of this parameter with the local RS magnitude.

Several series of RS measurements were performed. In a region where constant magnitude of Type I residual stress was expected, the deviation of the measured values from the mean are directly representative of the Type II + Type III residual stress sum. In addition, multiple measurements within a single grain provided an assessment of Type III residual stress alone.

The profile of residual stress variation across the beam represented the sum of all three types of residual stress. In this case, the Type II + Type III sum could also be extracted by comparison with the macro-scale profile provided by the simulation that was validated by matching the mean profile to the observation. The comparison between the simulated and experimental Type II+III RS fields was conducted using a statistical approach. The numerical simulation also allowed the abstraction of the sole Type III RS.

In the following sections, after presenting the details of this investigation and its results, we evaluate the dispersion of experimental data using 95% confidence interval and discuss the implications of the findings for structural integrity assessment.

2. Sample and Test Setup Description

Four-point bending experiment was performed on a miniature beam carefully machined from a plate of Aluminium alloy AA6082. The choice of material was made on the basis of grain size consideration (10-150 μ m) to enable multiple RS measurements within a grain.

The load applied during bending was precisely monitored to allow accurate calculation of the bending moment and the assessment of the attendant plastic deformation (eigenstrain) that generates the residual stress upon load release. In addition, the beam curvature was also monitored as an additional measure of consistency between FE numerical model and the sample macro-scale deformation response.

A schematic representation of the test is reported in Fig.2a along with the principal beam dimensions.

Microtest deformation stage by Deben Research (UK) is capable to applying forces up to 5kN. The test was performed under displacement control, and applied force and crosshead displacement were monitored (Fig.2b). Minor instabilities of deformation were observed at higher loads during the test (Fig.2b) that were associated with rearrangements within the contact regions between loading pins and sample. These occurred away from at the centre of the beam, and did not affect the deformation within the region of interest.

<< Figure 2 here >>

3. EBSD and FIB-DIC micro-ring-core analyses

Sample surface preparation was conducted using 400, 800 and 1200 grit grinding paper, followed by fine polishing in a water-based solution containing a suspension of 9 μ m, 3 μ m and 1 μ m diamond particles, followed by 0.1 μ m colloidal silica finishing as the last step. The underlying sample microstructure was analysed in terms of grain shape and orientation using EBSD.

In order to obtain representative statistical distribution of the underlying crystal orientation, texture analysis was conducted by collecting a large 2D EBSD map across the entire sample width of 0.5mm, as shown in Fig.2(a). This area was considered sufficiently large to obtain a statistically representative and robust description of crystallographic texture. EBSD results and pole figures are illustrated in Fig.3. A useful representation of material texture in the context of theoretical and numerical analysis (CP-FEM) is the use of the Orientation Distribution Function (ODF), depicted in Fig.3(c).

<< Figure 3 here >>

A second region selected for EBSD mapping, indicated in Fig.2(a) by the horizontally elongated red rectangle, was selected for the purpose of FIB-DIC micro-ring-core measurements.

FIB-DIC micro-ring-core measurement procedure consists of using Focused Ion Beam (FIB) for progressive milling of an annular trench-like feature. As milling advances, sequential images of the material surface are acquired with the purpose of tracking the evolution of the elastic displacements

taking place using DIC. Post processing of the obtained in-plane displacements field allows the evaluation of the relief strain profile that is fitted with a master-function derived by numerical simulation of the process. The outcome of fitting is the determination of the residual elastic strain that was present in the material prior the milling-induced relaxation. An additional calculation enables the assessment of residuals stress by linear combination of the in-plane residual elastic stress components through Hooke's law.

In order to facilitate DIC displacement tracking, a thin layer of Pt was deposited on the sample surface, exhibiting random features on the order of tens of nanometres in size after brief exposure to the focused ion beam for 'etching'. The FIB energy was set to 30keV for milling. The ring-core milling process was conducted in 40 steps, with $n=10$ SEM images collected at each milling with low dwell time. This procedure is known to minimise the effect of SEM imaging artefacts on strain assessment. The inner diameter of the ring-core was chosen to be $5\mu\text{m}$, meaning that the measurement approach adopted provided average values of RS within a gauge volume having this lateral extent and the depth up to approximately one third of the inner ring-core diameter [44].

The first series of RS measurement was performed at different locations at a distance of $\sim 40\mu\text{m}$ from the beam side surface along the y axis. Due to the uniformity of bending moment within the central region of the beam, continuum analysis predicts that Type I RS field is uniform within this area. For each measurement not only of the RS magnitude was evaluated, but also the associated error bar corresponding to 95% confidence range that was found using error propagation through the multiple steps of the analysis process (DIC tracking, strain fitting, and allowance being made for material elastic anisotropy [40, 45]).

The plot in Fig.4 presented the results of RS evaluation within specific grains that are indicated on the corresponding EBSD map that reveals the grain morphology and orientation (by colour), and also shows the FIB-DIC marker locations.

<< Figure 4 here >>

The positions of individual measurement identified by the black circles are numbered in the map in Fig.4(b). To help the identification of the grain to which each measurement belongs, the plot in Fig.4(a) reports the RS values using markers of the same colour as the associated grain in the EBSD map.

Fig.4 reveals that RS variation can be observed within individual grains (Type III, intragranular) and from grain to grain (Type II, intergranular) against the backdrop of the uniform Type I macrostress. The adjacent grains numbered I and II show significant difference in the mean RS magnitude, with the mean RS magnitude in grain II around 50MPa greater than that in grain I. The mean RS in grain III appears to lie between the values in grains I and II, but the spread for the three point measurements within grain III is much greater than for the four point measurements within grain I. This is clearly related to the greater magnitude of Type III intragranular RS in grain III. Finally, it is observed that the cluster of points for the measured RS values at this location is centred around the Type I macroscopic RS value predicted by the continuum simulation, as illustrate in Fig.5 for the values close to zero of the y-axis.

To investigate the RS variation further, the second series of FIB-DIC measurements were carried out at different positions along the y-axis across the beam cross-section, in accordance with the coordinate system shown in Fig.2. Fig.5 allows two observations to be made:

- (a) on the one hand, the overall shape of RS profile across a plastically bent beam is captured correctly. In particular, it can be noted that the sign of RS (tensile vs compressive) has been captured correctly. It is also interesting to note that the quality of agreement is particularly high within the elastic core of the beam, whilst in the near-surface regions that experienced large plastic bending strain the deviation observed is larger.
- (b) on the other hand, significant deviation from the macroscopic RS value is observed that is statistically meaningful, in that the predicted value lies outside the error bar that indicates 95% confidence interval.

<< Figure 5 here >>

When RS measurement data is considered, it may be tempting to associate to the observed scatter with errors associated with deficiencies of experimental setup or interpretation. The present results show that this may be a dangerous simplification: the deviation of measured values from expectation is likely to be caused by fine scale inhomogeneities of deformation (eigenstrain) giving rise to Type II and III residual stresses. The details of grain morphology such as size, shape, the nature of grain boundary, the relative (mis)orientation between neighbours and the attendant elastic-plastic anisotropy are well known

to have an impact of deformation mechanisms that is manifested not only at the microstructural level, but also at larger scale [46, 47].

The ease of plastic flow varies depending on the crystal lattice orientation with respect to the loading direction, giving rise to intergranular eigenstrain and the associated Type II RS as a consequence. Schmid factor is a well-known measure of the propensity of a single crystal of given orientation to undergo plastic slip under uniaxial loading. However, since the relevance of Schmid factor for polycrystals remains the subject of controversy, we present a brief discussion of this matter in the following sections.

Similarly, the development and evolution of inelastic deformation features such as slip bands within individual grains that are known to be affected by the grain shape lead to intragranular eigenstrains that give rise to Type III residual stresses.

Finally, it is important to note that Type II and III micro-scale residual stresses are no less physical than Type I macroscopic RS. Hence, procedures need to be developed to take correct account of these stresses in design against structural failure. To help answer these questions, in the following sections we present statistical analysis of RS distributions, and examine the correlation between Schmid factor and RS at the grain level.

4. Finite Element Analysis

4.1 Macro-scale simulation

The RS field arising due to inelastic bending was numerically evaluated using a three-dimensional non-linear deformation model. The simulation was subdivided into two steps (loading and unloading) in order to capture the residual stress. A refined mesh was used in the region of interest (central part of the beam) to ensure accuracy and reliability of the results. Computational time was optimised by using problem symmetry. Isotropic hardening was used, with the parameters calibrated by matching the macroscopic stress-strain curve.

The match between the beam curvature predicted by the simulation and the actual sample was verified by the graphical superposition of the real scale result onto the beam optical image at the maximum load (Fig.6). The beam curvature upon load release was also matched correctly. The deformed shape and contour plot are shown in the inset below the loaded sample image in Fig.6.

<< Figure 6 here >>

4.2 Crystal Plasticity simulation

The modelling of crystallographic plastic deformation was performed on the basis of the FE numerical simulation code that has been reported previously [48, 49]. A Representative Volume Element (RVE) in the form of a unit volume cube was discretised into a 3D (8x8x8) mapped mesh composed of C3D20 elements [50]. In the first instance, a Voronoi tessellation was performed to create a population of 600 grains with random crystal orientations. This model enabled the simulation of an untextured material.

The second simulation was performed with the aim of incorporating a more realistic material crystal orientation into the analysis. To this end, texture data obtained using EBSD was fed into the CP-FEM code. Correct implementation of the characteristic crystal orientation enhances the model fidelity considerably, and improves the accuracy of residual stress simulation. The RVE was populated with grains of different sizes to capture the large grain size variability found by EBSD analysis. Local crystal orientations were assigned in accordance with the ODF obtained experimentally, ensuring that the overall crystal texture of the sample is reproduced in the RVE.

In the present approach, grain boundaries were not modelled explicitly, in order to keep the computational effort practical. This approach was preferred over the simulation of the actual local morphology of the grains because the present study aims at the statistical description of the origins of residual stresses, and at validating the model that can be potentially used for prediction of residual stress where the underlying crystal morphology is unknown. In passing, it is worth noting that a number of studies are found in literature, where the actual grain morphology and orientation is accounted for in some detail [51-53].

Alongside aleatoric uncertainty introduced by neglecting the factors described above, another class of error source may play its relevant role, the epistemic uncertainty due to numerical errors [54]. Epistemic uncertainty cannot be described by a probability distribution and it originates from the presence of inaccuracy in the model itself, e.g. internal parameters in the model, round-off errors, and uncertainty in errors due to numerical algorithms.

In this model, the slip system hardening was described as follows:

$$h_{\alpha} = [q + (1 - q)\delta_{\alpha}]h \quad (2)$$

Where α identifies the active slip system, h is the self-hardening rate and q describes a latent hardening parameter, with values in the range $1 < q < 1.4$.

The elastic and plastic parameters of the material studied were taken from literature: anisotropic stiffness coefficients $C_{11} = 108GPa$, $C_{12} = 61GPa$ and $C_{22} = 29GPa$ [55], and the Critical Resolved Shear Stress (CRSS) $\tau_c = 142.9MPa$ [56]. The hardening parameters were calibrated in the course of simulation to obtain agreement with macro-scale model behaviour.

Periodic and symmetry conditions were imposed to the RVE as boundary conditions. In order to emulate the material loading history, a macro-scale FEM model was employed. At the appropriate relevant instant in the loading history, the strain imposed by the macro-scale model were transferred to the micro-scale model by imposing the equivalent displacements to the RVE. Iterative refinement of the hardening parameters was performed to match the average RVE stress value to the local stress value from macro-scale FEM simulation. In what follows, and for the purpose of comparison with the experiments, the RVE was chosen to lie in the outer-most region of the beam that undergoes compression during bend loading, as indicated in Fig.7 which shows the stress distribution at two stages of loading for both macro- and micro-scale models. This Figure shows the CP-FEM contour plot of the un-textured RVE.

<< Figure 7 here >>

The comparison of the statistical distributions of stress values within the RVE with that obtained from experimental measurements is reported in §5.

5. Statistical Analysis of RS Distribution

In accordance with eq. (3) we perform a point-wise calculation of Type II+III RS as follows:

$$\sigma_i^{RS,II+III} = \sigma_i - \sigma_i^{RS,I} \quad (3)$$

Here $\sigma_i^{RS,II+III}$ denote the deviation of RS from the macroscopic average value that corresponds to Type II and III combination, and is calculated as the difference between σ_i , the total RS measured at

point i , and $\sigma_i^{RS,I}$ that denotes the macroscopic Type I RS extracted from the simulation result for the same position where σ_i measurement was performed.

The data for Type II+III RS was processed and represented in the form of a histogram shown in Fig.8. It was found that, to the first approximation justified by the quality and amount of the data available, the distribution of $\sigma^{RS,II+III}$ RS values conforms well to a Gaussian distribution that is shown in Fig.8 by the dash-dot curve. Further accumulation of detailed data may reveal intricacies of statistical distributions.

At this stage it is worth mentioning that our finding is consistent with reports for ‘live’ stress by other authors [57, 58] who drew their conclusions from HR-EBSD analysis of micro-scale stress within a specimen subjected to external uniaxial load.

For the purposes of Uncertainty Quantification (UQ) incorporation in design on the basis of continuum simulation it may be required to incorporate the presence of Type II+III RS in the overall assessment of statistical deviation from the macroscopic RS prediction. Previously, UQ has been reported for experimental RS evaluation using FIB-DIC procedures [40, 45]. This procedural error can be amalgamated with the uncertainty that arises from the deviation between the actual RS values and macroscopic description, i.e. $\sigma_i^{RS,II+III}$.

The standard deviation of experimental data for the totality of measurement points is found as:

$$S''_{\sigma^{RS,II+III}} = \sqrt{\frac{1}{n_1 - 1} \sum_{i=1}^{n_1} (S_{\sigma_i})^2} \quad (4)$$

where S_{σ_i} is the standard deviation for each experimental FIB-DIC point, and n_1 is the number of experimental points.

The dispersion of the actual residual stress values from macroscopic predictions can be assessed by calculating the standard deviation as follows:

$$S'_{\sigma^{RS,II+III}} = \sqrt{\frac{1}{n_1 - 1} \sum_{i=1}^{n_1} (\sigma_i^{RS,II+III})^2} \quad (5)$$

where n_1 is the number of measurements.

The overall standard deviation can be evaluated by combining the above as follows:

$$S_{\sigma_{RS,II+III}} = S''_{\sigma_{RS,II+III}} + S'_{\sigma_{RS,II+III}} \quad (6)$$

Thus obtained, $S_{\sigma_{RS,II+III}}$ was used to define the confidence band that describes the variability of RS values around the continuum macroscopic predictions. At each position i across the beam, the confidence limits were defined as follows:

$$[\sigma_i^{RS,I} - z^* S_{\sigma_{RS,II+III}}; \sigma_i^{RS,I} + z^* S_{\sigma_{RS,II+III}}] \quad (7)$$

where z^* is the critical value related to the required confidence level. To attain the confidence level of 95% the value of z^* needs to be set to 1.96. On the basis of the above calculations, S_{σ} value of 53 MPa was found.

The statistical distribution of the RS II+III stresses can be visualised graphically for both the numerical simulation results (CP-FEM) and experimental evaluation (FIB-DIC), as illustrated in Fig.7(a) and (b), respectively. RS II+III stress values from CP-FEM simulation were obtained by collecting the stress values at integration points and subtracting the mean RVE value, according to eq. (3).

The information regarding Type III RS was extracted solely from the CP-FEM simulation, as follows: RS Type II+III values at the integration point j belonging to grain k were calculated using (3), and the mean value for the specific grain (Type II) was subtracted:

$$\sigma_{jk,CP-FEM}^{RS,III} = \sigma_{jk,CP-FEM}^{RS,II+III} - \frac{1}{N} \sum_j \sigma_{jk,CP-FEM}^{RS,II+III} \quad (8)$$

where N is the number of integration points within grain k .

Type III RS standard deviation for the entire RVE could be evaluated as:

$$S_{\sigma_{CP-FEM}^{RS,III}} = \sqrt{\frac{1}{n_1 - 1} \sum_{i=1}^{n_1} (\sigma_{jk,CP-FEM}^{RS,III})^2} \quad (9)$$

This calculation allowed the quantification of Type III RS standard deviation, that turned out to be 66MPa and 56MPa, respectively for the untextured and textured polycrystalline materials.

<< Figure 8 here>>

For the purpose of comparison, the values of standard deviations are in the bar chart in Fig.9.

<< Figure 9 here>>

<< Table 1 here>>

It is apparent from the plots presented in Fig.9 that a wider distribution (by ~45%) was obtained by the CP-FEM simulation compared to the experimental measurements (RS Type II+III), concerning the untextured polycrystalline material. When the measurement error propagation is accounted, the difference in the Gaussian widths reduces to ~29%, but persists. On the other hand, if the actual texture of the polycrystalline material is considered, RS Type II+III shows a smaller difference compared to the experimental result (~24%). A reduction of the RS standard deviation was experienced also regarding the sole Type III RS; considering the material texture, the gaussian width reduced of ~15%.

The discrepancy between CP-FEM model prediction and experiment measurements highlights the fact that matching the macro-scale (Type I) RS is insufficient for obtaining a statistically representative Type II+III description to underlie subsequent in-service modelling. However, the experimental findings show a relatively large uncertainty due to the nature of the experimental technique itself. It is therefore worth noting that the confidence interval is very close to the values attained through the numerical simulation, therefore acceptable matching was found overall. This hints that in order to obtain a better representation of RS Type II+III distributions, the accounting of grain boundaries and defects, etc might play their role. Furthermore, since rolling was employed to produce the alloy plate studied here, we surmise that the material inherited not only the grain structure, but also the pre-existing RS state from prior processing history.

Type III RS evaluated through the numerical simulation highlighted a narrower distribution compared to the sum Type II+III as expected.

Using the confidence band defined according to (7), the plot in Fig.10 was constructed that reports the macroscopic RS prediction (solid curve) and the correspondent confidence band indicated by the two dashed curves. Furthermore, all experimental points are also included with their respective error bars. The Gaussian distribution function shown by the inset illustrates how Type II+III RS cause a spread around the mean Type I RS value at any position across the beam.

<< Figure 10 here >>

It is evident that all experimental points lie within the band that corresponds to 95% confidence level, supporting the validity of the proposed approach. It is worth noting the relative magnitudes of Type II+III residual stresses, on the one hand, and of Type I stresses, on the other. The half width of the band magnitude (54MPa) is comparable with Type I RS magnitudes, so that the presence of the finer scale RS may mean that the actual stress at any given location may differ in sign from the prediction.

This representation of RS point values by statistical distributions is potentially great significance for structural integrity and reliability design of mechanical systems, in that it can underpin design based on the appropriate confidence level selected for specific applications. Considering for instance a hypothetical problem of design against crack nucleation, whereas high structural integrity reliability is sought, the employed RS should be that that consider a worse-case scenario (i.e. upper limit with a certain confidence). In the same way, whereas high performance is required, a less conservative approach can be chosen being, again, aware of the probabilistic occurrence of an adverse event.

6. Influence of the Crystal Orientation on RS Development

It is well known that the crystal plasticity activity is highly dependent on the local orientation of the material, besides the external load applied [59, 60]. In fact, in all the crystalline structures there is always a specific slipping plane that is more prone to resolve shear stress. Such slip plane can be described upon knowledge of the so-called Schmid factor with regards to the loading direction. According to the Schmid's law, the amount of shear stress that can be resolved is:

$$\tau = \sigma \cdot m \quad (10)$$

where σ identifies the external load and m is the Schmid factor. The latter is defined as:

$$m = \cos(\phi) \cos(\lambda) \quad (11)$$

where ϕ is the angle between the loading direction and the slip plane normal, and λ is the angle between the slip plane normal and the slip direction. For crystals with fcc lattice there are 12 equivalent slip systems of the $(111) < 1\bar{1}0 >$ type available. Since the onset of slip occurs on the system with the highest resolved shear stress, calculation of m must be performed for each system, and the greatest value selected.

Since full crystal orientation is available for each grain from the EBSD map acquired, Schmid factor with respect to the loading direction can be calculated for each measurement point. The details of sample orientation are reported in the Appendix.

The purpose of abstracting the Schmid factors was the understanding of the nature of measured RS deviation from the macroscopic stress. According to the Schmid's law, grains exhibiting high values of Schmid factor are more prone to undergo to plastic deformation and, in turns, will generate higher values of residual stress. The plot in Fig.11 shows the direct comparison of the $\Delta\sigma_i$ quantities with the corresponding Schmid factor values. The dotted lines are polynomial fits that serve as guide to facilitate the visualisation of the trends behaviour.

<< Figure 11 here >>

The comparison of the two curves in Fig.11 suggests the existence of a correlation between the two quantities, the orientation dependent Schmid factor of a given grain, on the one hand, and Type II+III RS, $\Delta\sigma$, on the other. Indeed, the lower values of Schmid factor in the middle region appear to match well the lower values of the absolute magnitude $|\sigma_i^{RS,II+III}|$ of Type II+III RS. This compares favourably with reported unsuccessful attempts to find correlation between Schmid factor and total RS value, $\sigma^{RS} = \sigma^{RS,I} + \sigma^{RS,II} + \sigma^{RS,III}$. Rational analysis of the correlation suggests that best correlation is likely to be found when only Type II RS component is used, $\sigma^{RS,II}$. Nevertheless, it is worth noting that the

deformation response of grain is strongly affected by the neighbouring grains, setting a limit to the validity of Schmid factor as a universal correlating parameter. In turns, locally the stress state is no longer uniaxial but rather multiaxial, leading to an inaccurate quantification of slip activity using this approach. This is also repeatedly highlighted in [57] where a “true” Schmid factor is evaluated in order to account the actual stress state acting in the considered grain.

7. Conclusions

Type I, II and III RS measurements conducted by FIB-DIC at the grain-level show a significant degree of scatter. Consideration of the results revealed that to a great extent this scatter can be interpreted as a statistical distribution of Type II and III residual stresses. Statistical description of Type II+III RS dispersion around the macroscopic Type I value was proposed.

The principal outcomes of the present study of intra- and inter-granular Type II+III RS were:

1. Overall, the mean values of the measured residual stresses follow closely the macroscopic continuum Type I RS variation predicted by the numerical model calibrated against the macroscopic stress-strain curve of the material and incorporating appropriate description of hardening.
2. A series of measurements was conducted at a location where the nominal macroscopic Type I residual stress was constant. The results revealed significant scatter in both inter-granular Type II RS, and intra-granular Type III RS. It was confirmed that the range of spread of Type II+III RS values can be as large as the Type I residual stress value itself.
3. The Type II+III RS statistical distribution of the measured stress from the nominal macroscopic value by the continuum model was found to conform well to Gaussian statistics. Based on the data collected, the breadth of this distribution was found to be of the order of ~41MPa.
4. Error propagation that incorporates FIB-DIC measurement inaccuracies was used to assess the 95% confidence interval that corresponds to Gaussian statistics with the breadth of ~53MPa. This is consistent with the result reported above, and incorporates the contribution from the measurement error.

The statistical distributions of RS obtained by experiment and numerical modelling found 29% of disagreement if a randomly distributed crystal structure is simulated, whilst

whereas a realistic crystal texture of the material is accounted this disagreement drops to 24%. The mismatch is thought mainly due to the pre-existing RS state from prior processing history, beside minor simplifications adopted in the CP-FEM model (e.g. no grain boundary). However, other sources of errors may be relevant. As highlighted in [53], the overall stress state might significantly depend on the 3D morphology of the grains below the free surface, over a thickness of at least twice the average grain size. This can be considered as a supplementary error source. Moreover, a further cause of error may be of epistemic type. As highlighted in section 4.2, epistemic uncertainty are not due to physical causes but rather to numerical inaccuracy [54]. All the listed causes concur in the generation of the mismatch experienced between numerical and experimental results.

5. Type III RS evaluated by CP-FEM simulation showed a standard deviation of the distribution of 66 MPa and 56 MPa, respectively for the untextured and textured CP-FEM simulations.
6. Analysis of the local Schmid factor showed a limited correlation with the Type II+III RS scatter. The origin of Type II+III RS deviation from Type I macroscopic prediction is thought to be due to the multiaxial stress state induced by the microstructure and nearest neighbour grain interaction.
7. The results obtained have significant implications for design, in that they reveal the magnitude of grain level RS variation and provide an improved basis for rational design that incorporates statistical information and allows reliable uncertainty quantification.

Acknowledgements

AMK acknowledges funding received for the MBLEM laboratory at Oxford through EU FP7 project iSTRESS (604646), and access to the facilities at the Research Complex at Harwell (RCaH), under the Centre for In-situ Processing Studies (CIPS). The authors declared no conflict of interest.

Appendix – orientation convention for Schmid factor calculation

Laboratory (EBSD) coordinate system is shown in Fig.12 together with sample geometry. The loading direction corresponds to the z -axis direction (also denoted RD in the EBSD system). Schmidt factor is evaluated for loading in the z -direction for all slip systems of the $(111) < \bar{1}\bar{1}0 >$ type.

<< Figure 12 here >>

References

1. Soleymani, M., M.H. Parsa, and H. Mirzadeh, *Molecular dynamics simulation of stress field around edge dislocations in Aluminum*. Computational Materials Science, 2014. **84**: p. 83-96.
2. Lin, Z.C., J.C. Huang, and Y.C. Chao, *The study of deformation and stress—strain distribution of nano-scale thin sheet copper under the biaxial tensile loads by using molecular dynamics and finite-element method*. Proceedings of the Institution of Mechanical Engineers, Part C: Journal of Mechanical Engineering Science, 2008. **222**(6): p. 1097-1107.
3. Salehinia, I., et al., *Molecular dynamics simulations of plastic deformation in Nb/NbC multilayers*. International Journal of Plasticity, 2014. **59**: p. 119-132.
4. Shen, S. and S.N. Atluri, *Atomic-level Stress Calculation and Continuum-Molecular System Equivalence*. cmes, 2004. **6**(1): p. 13.
5. Zhou, M., *A new look at the atomic level virial stress: on continuum-molecular system equivalence*. Proceedings of the Royal Society of London. Series A: Mathematical, Physical and Engineering Sciences, 2003. **459**(2037): p. 2347-2392.
6. Macherauch, E., H. Wohlfahrt, and U. Wolfstieg, *Zur zweckmässigen Definition von Eigenspannungen*. HTM, 1973. **28**: p. 201.
7. Pintschovius, L., et al., *Residual stress measurements by means of neutron diffraction*. Materials Science and Engineering, 1983. **61**(1): p. 43-50.
8. Macherauch, E., *INTRODUCTION TO RESIDUAL STRESS A2 - NIKU-LARI, A, in Residual Stresses*. 1987, Pergamon. p. 1-36.
9. Mughrabi, H., *On the role of strain gradients and long-range internal stresses in the composite model of crystal plasticity*. Materials Science and Engineering: A, 2001. **317**(1): p. 171-180.
10. Mughrabi, H., *Dislocation wall and cell structures and long-range internal stresses in deformed metal crystals*. Acta Metallurgica, 1983. **31**(9): p. 1367-1379.
11. Korsunsky, A.M., *Variational eigenstrain analysis of synchrotron diffraction measurements of residual elastic strain in a bent titanium alloy bar*. Journal of Mechanics of Materials and Structures, 2006. **1**(2): p. 18.
12. Korsunsky, A.M., *The modelling of residual stresses due to surface peening using eigenstrain distributions*. The Journal of Strain Analysis for Engineering Design 2005. **40**(8): p. 7.
13. Jun, T.-S. and A.M. Korsunsky, *Evaluation of residual stresses and strains using the Eigenstrain Reconstruction Method*. International Journal of Solids and Structures, 2010. **47**(13): p. 1678-1686.
14. DeWald, A.T. and M.R. Hill, *Eigenstrain-based model for prediction of laser peening residual stresses in arbitrary three-dimensional bodies Part 2: Model verification*. The Journal of Strain Analysis for Engineering Design, 2009. **44**(1): p. 13-27.

15. Salvati, E., et al., *Eigenstrain Reconstruction of Residual Strains in an Additively Manufactured and Shot Peened Nickel Superalloy Compressor Blade*. Computer Methods in Applied Mechanics and Engineering, 2017.
16. Wang, Z., H. Yu, and Q. Wang, *Analytical solutions for elastic fields caused by eigenstrains in two joined and perfectly bonded half-spaces and related problems*. International Journal of Plasticity, 2016. **76**: p. 1-28.
17. Liu, S., et al., *Analytical solution for elastic fields caused by eigenstrains in a half-space and numerical implementation based on FFT*. International Journal of Plasticity, 2012. **35**: p. 135-154.
18. Cuddihy, M.A., et al., *On cold dwell facet fatigue in titanium alloy aero-engine components*. International Journal of Fatigue, 2017. **97**: p. 177-189.
19. Nibennanoun, Z., et al., *Improving diamond coating on Ti6Al4V substrate using a diamond like carbon interlayer: Raman residual stress evaluation and AFM analyses*. Diamond and Related Materials, 2012. **22**: p. 105-112.
20. Bull, S.J. and A.M. Korsunsky, *Mechanical properties of thin carbon overcoats*. Tribology International, 1998. **31**(9): p. 547-551.
21. Pratihari, S., et al., *Neutron diffraction residual stress measurements in a 316L stainless steel bead-on-plate weld specimen*. International Journal of Pressure Vessels and Piping, 2009. **86**(1): p. 13-19.
22. Korsunsky, A.M., K.E. Wells, and P.J. Withers, *Mapping two-dimensional state of strain using synchrotron X-ray diffraction*. Scripta Materialia, 1998. **39**(12): p. 1705-1712.
23. Korsunsky, A.M., K.E. James, and M.R. Daymond, *Intergranular stresses in polycrystalline fatigue: diffraction measurement and self-consistent modelling*. Engineering Fracture Mechanics, 2004. **71**(4-6): p. 805-812.
24. Korsunsky, A.M., M.R. Daymond, and K.E. James, *The correlation between plastic strain and anisotropy strain in aluminium alloy polycrystals*. Materials Science and Engineering A, 2002. **334**(1-2): p. 41-48.
25. Salvati, E., et al., *Elucidating the Mechanism of Fatigue Crack Acceleration Following the Occurrence of an Underload Advanced Engineering Material*. 2016.
26. Salvati, E., et al., *Separating plasticity-induced closure and residual stress contributions to fatigue crack retardation following an overload*. Journal of the Mechanics and Physics of Solids, 2017. **98**: p. 222-235.
27. Kassner, M.E., P. Geantil, and L.E. Levine, *Long range internal stresses in single-phase crystalline materials*. International Journal of Plasticity, 2013. **45**: p. 44-60.
28. Guo, Y., et al., *Growth of $\{ \}$ twins in titanium: A combined experimental and modelling investigation of the local state of deformation*. Acta Materialia, 2017. **126**: p. 221-235.
29. Britton, T.B. and A.J. Wilkinson, *High resolution electron backscatter diffraction measurements of elastic strain variations in the presence of larger lattice rotations*. Ultramicroscopy, 2012. **114**: p. 82-95.
30. Britton, T.B. and A.J. Wilkinson, *Measurement of residual elastic strain and lattice rotations with high resolution electron backscatter diffraction*. Ultramicroscopy, 2011. **111**(8): p. 1395-1404.
31. Jiang, J., T.B. Britton, and A.J. Wilkinson, *Measurement of geometrically necessary dislocation density with high resolution electron backscatter diffraction: Effects of detector binning and step size*. Ultramicroscopy, 2013. **125**: p. 1-9.
32. Jiang, J., T.B. Britton, and A.J. Wilkinson, *Evolution of dislocation density distributions in copper during tensile deformation*. Acta Materialia, 2013. **61**(19): p. 7227-7239.
33. Jiang, J., T.B. Britton, and A.J. Wilkinson, *The orientation and strain dependence of dislocation structure evolution in monotonically deformed polycrystalline copper*. International Journal of Plasticity, 2015. **69**: p. 102-117.
34. Kartal, M.E., R. Kiwanuka, and F.P.E. Dunne, *Determination of sub-surface stresses at inclusions in single crystal superalloy using HR-EBSD, crystal plasticity and*

- inverse eigenstrain analysis*. International Journal of Solids and Structures, 2015. **67–68**: p. 27-39.
35. Zhang, Y., et al., *Validation of the Contour Method of Residual Stress Measurement in a MIG 2024 Weld by Neutron and Synchrotron X-ray Diffraction*. Journal of Neutron Research, 2003. **11**(4): p. 181-185.
 36. Hill, M.R. and M.D. Olson, *Repeatability of the Contour Method for Residual Stress Measurement*. Experimental Mechanics, 2014. **54**(7): p. 1269-1277.
 37. Schuster, S. and J. Gibmeier, *Incremental Hole Drilling for Residual Stress Analysis of Strongly Textured Material States – A New Calibration Approach*. Experimental Mechanics, 2016. **56**(3): p. 369-380.
 38. Schajer, G.S., B. Winiarski, and P.J. Withers, *Hole-Drilling Residual Stress Measurement with Artifact Correction Using Full-Field DIC*. Experimental Mechanics, 2013. **53**(2): p. 255-265.
 39. Wolf, H. and W. Bohm, *The Ring-Core Method for Measuring Residual Stresses and its Use with Turbines and Generator Shafts*. Archiv. Eisenhiittenwesen 1971. **41**: p. 5.
 40. Lunt, A.J.G. and A.M. Korsunsky, *A review of micro-scale focused ion beam milling and digital image correlation analysis for residual stress evaluation and error estimation*. Surface and Coatings Technology, 2015. **283**: p. 373-388.
 41. Korsunsky, A.M., M. Sebastiani, and E. Bemporad, *Focused ion beam ring drilling for residual stress evaluation*. Materials Letters, 2009. **63**(22): p. 1961-1963.
 42. Salvati, E., et al., *The effect of eigenstrain induced by ion beam damage on the apparent strain relief in FIB-DIC residual stress evaluation*. Materials & Design, 2016. **92**: p. 649-658.
 43. Arnold, T., et al., *Ultra-precision surface finishing by ion beam and plasma jet techniques—status and outlook*. Nuclear Instruments and Methods in Physics Research Section A: Accelerators, Spectrometers, Detectors and Associated Equipment, 2010. **616**(2–3): p. 147-156.
 44. Salvati, E., et al., *An Investigation of Residual Stress Gradient Effects in FIB-DIC Micro-Ring-Core Analysis*. 2015.
 45. Salvati, E., T. Sui, and A.M. Korsunsky, *Uncertainty quantification of residual stress evaluation by the FIB-DIC ring-core method due to elastic anisotropy effects*. International Journal of Solids and Structures, 2016. **87**: p. 61-69.
 46. Zhao, H., B.P. Wynne, and E.J. Palmiere, *Effect of austenite grain size on the bainitic ferrite morphology and grain refinement of a pipeline steel after continuous cooling*. Materials Characterization, 2017. **123**: p. 128-136.
 47. Li, Y., et al., *The Influences of Grain Size and Morphology on the Hot Tearing Susceptibility, Contraction, and Load Behaviors of AA7050 Alloy Inoculated with Al-5Ti-1B Master Alloy*. Metallurgical and Materials Transactions A: Physical Metallurgy and Materials Science, 2016. **47**(8): p. 4024-4037.
 48. Song, X., et al., *Finite element modelling and diffraction measurement of elastic strains during tensile deformation of HCP polycrystals*. Computational Materials Science, 2008. **44**(1): p. 131-137.
 49. Korsunsky, A.M., et al., *Comparative assessment of dissipated energy and other fatigue criteria*. International Journal of Fatigue, 2007. **29**(9–11): p. 1990-1995.
 50. Simulia, *ABAQUS User Manual*. 2015
 51. Zeghadi, A., et al., *Ensemble averaging stress-strain fields in polycrystalline aggregates with a constrained surface microstructure-part 1: Anisotropic elastic behaviour*. Philosophical Magazine, 2007. **87**(8-9): p. 1401-1424.
 52. Lim, H., et al., *Grain-scale experimental validation of crystal plasticity finite element simulations of tantalum oligocrystals*. International Journal of Plasticity, 2014. **60**: p. 1-18.
 53. Zeghadi, A., et al., *Ensemble averaging stress–strain fields in polycrystalline aggregates with a constrained surface microstructure –Part 2: crystal plasticity*. Philosophical Magazine, 2007. **87**(8-9): p. 1425-1446.

54. Chernatynskiy, A., S.R. Phillpot, and R. Lesar, *Uncertainty quantification in multiscale simulation of materials: A prospective*, in *Annual Review of Materials Research*. 2013. p. 157-182.
55. Courtney, T.H., *Mechanical Behavior of Materials*, 1990.
56. Saai, A., et al., *Crystal plasticity finite element simulations of pure bending of aluminium alloy AA7108*. *International Journal of Material Forming*, 2016. **9**(4): p. 457-469.
57. Wan, V.V.C., et al., *An HR-EBSD and computational crystal plasticity investigation of microstructural stress distributions and fatigue hotspots in polycrystalline copper*. *Acta Materialia*, 2016. **115**: p. 45-57.
58. Jiang, J., T.B. Britton, and A.J. Wilkinson, *Mapping type III intragranular residual stress distributions in deformed copper polycrystals*. *Acta Materialia*, 2013. **61**(15): p. 5895-5904.
59. Pinna, C., et al., *Assessment of crystal plasticity finite element simulations of the hot deformation of metals from local strain and orientation measurements*. *International Journal of Plasticity*, 2015. **73**: p. 24-38.
60. Hama, T., A. Kobuki, and H. Takuda, *Crystal-plasticity finite-element analysis of anisotropic deformation behavior in a commercially pure titanium Grade 1 sheet*. *International Journal of Plasticity*.